PAPER

Nanomechanical mapping in air or vacuum using multi-harmonic signals in tapping mode atomic force microscopy

To cite this article: Nurul Huda Shaik et al 2020 Nanotechnology 31 455502

View the article online for updates and enhancements.

Recent citations

 Nanomechanical mapping of soft materials with the atomic force microscope; methods, theory and applications Ricardo Garcia



IOP ebooks™

Bringing together innovative digital publishing with leading authors from the global scientific community.

Start exploring the collection-download the first chapter of every title for free.

IOP Publishing Nanotechnology

Nanotechnology 31 (2020) 455502 (17pp)

https://doi.org/10.1088/1361-6528/ab9390

Nanomechanical mapping in air or vacuum using multi-harmonic signals in tapping mode atomic force microscopy

Nurul Huda Shaik¹, Ronald G Reifenberger² and Arvind Raman¹

- ¹ School of Mechanical Engineering, Purdue University, West Lafayette, Indiana, 47907, United States of America.
- ² Department of Physics, Purdue University, West Lafayette, Indiana, 47907, United States of America.

E-mail: raman@purdue.edu

Received 24 February 2020, revised 13 April 2020 Accepted for publication 15 May 2020 Published 18 August 2020



Abstract

We present a method by which multi-harmonic signals acquired during a normal tapping mode (amplitude modulated) AFM scan of a sample in air or vacuum with standard microcantilevers can be used to map quantitatively the local mechanical properties of the sample such as elastic modulus, adhesion, and indentation. The approach is based on the observation that during the tapping mode operation in air or vacuum, the 0th and 2nd harmonic signals of microcantilever vibration are encountered under most operating conditions and can be mapped with sufficient signal to noise ratio. By measuring the amplitude and phase of the driven harmonic as well as the 0th and 2nd harmonic observables, we find analytical/semi-analytical formulas that relate these multi-harmonic observables to local mechanical properties for several classical tip-sample interaction models. Least squares estimation of the local mechanical properties is performed pixel by pixel. The method is validated through computations as well as experimental data acquired on a polymer blend made of Polystyrene and Polyolefin elastomer.

Supplementary material for this article is available online

Keywords: multi-harmonic, atomic force microscopy, compositional mapping, polymer characterization, surface properties, nonlinear dynamics

1

(Some figures may appear in color only in the online journal)

1. Introduction

Recent advances in dynamic AFM have enabled the excitation and measurement of the AFM microcantilever vibration at multiple frequencies. These multi-frequency AFM methods [1–11] help to better understand the interaction forces between the tip and the sample and lead to estimations of the local physical properties of the sample quantitatively with high resolution and high speed.

Multi-frequency AFM methods for nanomechanics began in the context of tapping mode or amplitude modulation AFM (AM-AFM) but have faced some key challenges. In AM-AFM a single eigenmode of the microcantilever is excited at resonance and higher harmonics of the driving frequency arise in the microcantilever spectrum due to the non-linearity of tip-sample interaction forces [12–24]. The bifurcations and stability of microcantilever motions in AM-AFM are very well understood [25, 26]. In principle, the acquisition of a large number of higher harmonics (> 20) in AM-AFM can be used to reconstruct the non-linear interaction forces [27]. In practice, however, the signal to noise ratio of these higher harmonics is generally poor [28, 29] as the harmonic number increases making it difficult to recover the high frequency components of the interaction forces. To overcome these issues, new designs such as torsional harmonic cantilevers [30–32], cantilevers with interdigitated high bandwidth fingers [33–37] and embedded low frequency paddles [38] have been proposed. However the use of

specialized microcantilevers impedes widespread adoption in the community.

In response to these challenges multi-frequency excitation methods have emerged recently where the microcantilever is excited with multiple frequencies in the resonance bandwidth of one or more eigenmodes. In these methods the microcantilever vibration observables at various frequencies can be acquired with higher signal to noise ratio. These methods include multi-modal excitation [3–8], such as bimodal [3–7] and trimodal [8] excitation, band excitation [9] and intermodulation AFM [10, 11]. Methods to convert multi-frequency observables into quantitative nanomechanical mapping have also been developed [30, 32, 36, 37, 39, 40]. However, the bifurcations and stability of microcantilever motions while using multi-frequency excitation remain poorly understood [41, 42].

In this article we re-examine the use of multi-harmonic AFM for nanomechanical mapping within the context of tapping mode/AM-AFM. There are many reasons to re-consider this problem, since AM-AFM remains the most widely used dynamic AFM mode and it is relatively easy for an average AFM user to understand its operation. Also, the bifurcations and stability of periodic motions in AM-AFM are well understood [12–24]. Finally, while many higher harmonics in AM-AFM have small signal to noise ratio, some harmonics such as the 0th, 2nd and 3rd harmonics appear quite frequently in AM-AFM on a variety of samples with sufficient signal to noise ratio. Still a method is needed to use a small subset of AM-AFM higher harmonics with sufficient signal to noise ratio in order to quantitatively estimate local nanomechanical properties.

Recently, there has been an effort towards the 'frugal' use of multi-harmonics where only a few, 0th, 1st, 2nd and perhaps 3rd harmonic in tapping mode/AM AFM are used to quantitatively map the local mechanical properties on the sample [43, 44]. The idea is to choose the values of nanomechanical parameters such as elastic modulus, viscoelasticity, adhesion, and indention of some analytical/semi-analytical contact mechanics model in a way to best match the experimental observables. Because only a small set of nanomechanical parameters need to be determined, it is sufficient to measure and map only a small subset of multi-harmonic amplitudes and phases. However, this approach has been only demonstrated on samples in liquids [43, 44] where the multiharmonic observables are much stronger due to the low Qfactors. Moreover, only simple tip-sample interaction models have been considered. If in fact the multi-harmonic approach could be extended to tapping mode/AM-AFM with standard microcantilevers in air/vacuum, and to a wide variety of tipsample interaction models then multi-harmonic AFM based on tapping mode/AM-AFM could become widely used for nanomechanical mapping.

In the current work, we present a generalized theoretical framework linking multi-harmonic observables in AM-AFM such as force harmonics to the physical properties of the sample. Since the origin of the higher harmonics is the non-linearity inherent in the tip-sample interaction, we develop such relationships for several commonly used contact

mechanics models such as DMT (Derjaguin-Muller-Toporov), Hertz and linear stiffness with adhesion. We then develop a least squares approach to extract the physical parameter values of the chosen contact mechanics model from a small subset of multi-harmonic observables such as the amplitudes and phases of the 0th, 1st and 2nd harmonic, or the 1st, 2nd and 3rd harmonic etc. The analytical/semi-analytical relationships and the parameter extraction approach are validated using direct numerical simulation of the AFM microcantilever interacting with samples with different moduli. An experimental approach for calibrating and correcting the 2nd harmonic amplitude and phase lag information in experiments is developed and presented. We then present experimental results on a polystyrene - low density polyethelene blend (PS-LDPE) [45] and map the elastic modulus, adhesion, indentation during a single AM-AFM scan using a standard microcantilever with less than 10% relative residual norm error over the scan. The approach opens up the possibility of using a small set of multi-harmonic observables during standard tapping mode/AM-AFM scans in air/vacuum for quantitative nanomechanical mapping of heterogeneous samples.

2. Multi-harmonic AFM theory

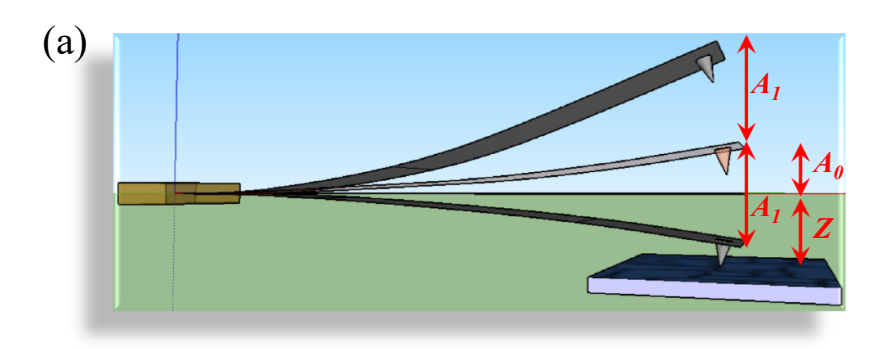
We derive here the general theory that rigorously connects multi-harmonic amplitudes and phases in tapping mode/AM-AFM to the interaction force harmonics. We then provide analytical/semi-analytical relations that link those force harmonics to physical properties of the sample.

We start by assuming a single-degree-of-freedom model for the microcantilever operating in AM-AFM mode. This assumption is valid as long as the first few harmonics are used as demonstrated with some simulation data in the supplementary material (stacks.iop.org/NANO/31/455502/mmedia). The single-degree-of-freedom equation of motion governing the tip motion q(t) of the resonant eigenmode of the microcantilever in AM-AFM when it interacts with the sample is given by

$$\frac{\ddot{q}}{\omega_{far}^2} + q + \frac{1}{\omega_{far}Q_{far}}\dot{q} = \frac{F_{dr}\cos(\omega_{dr}t) + F_{ts}(Z + q, \dot{q})}{k_{far}}, \quad (1a)$$

$$F_{ts}(Z+q,\dot{q}) = F_{ts,CONS}(Z+q) + F_{ts,DISS}(Z+q,\dot{q}). \tag{1b}$$

Here q(t), the generalized coordinate of the driven eigenmode is also the tip motion due to microcantilever deflection since the eigenmode is normalized such that its magnitude is unity at the free end [46] and F_{ts} is the tip sample-interaction force. This force is assumed to decompose additively into a conservative (tip sample gap dependent) $F_{ts,CONS}$ and a dissipative component $F_{ts,DISS}$ [47] or as referred to as even and odd components of interaction force [48]. F_{dr} is the magnitude of the modal excitation force. Z is the height of the unperturbed tip position with respect to the sample, and equals the Z-piezo displacement modulo, a constant (see figure 1).



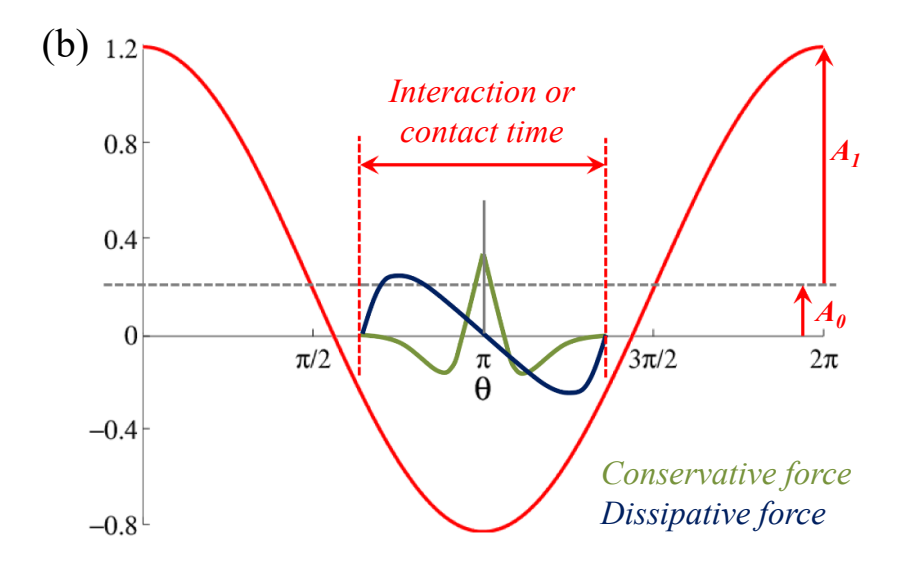


Figure 1. (a) A schematic of an oscillating microcantilever showing the key motion or displacement variables. The schematic emphasizes the average deflection of the tip A_0 , which is generally significant compared to the set-point amplitude of the drive harmonic A_1 . (b) A schematic of the time history of the tip motion (in terms of θ) to the leading order, along with the conservative and dissipative tip-sample interaction forces encountered by the tip during this motion.

Furthermore ω_{far} , Q_{far} , and k_{far} are respectively the natural frequency, the quality factor and the calibrated stiffness of the fundamental mode of the microcantilever, which are typically measured while the microcantilever is withdrawn from the sample. In what follows, we derive and express the tip sample force harmonics in terms of multi-harmonic microcantilever vibration observables based on the assumption that the tip motion q(t) is periodic while the tip is interacting with the sample.

2.1. Relationship between multi-harmonic observables and tip-sample force harmonics

Let the steady state motion of the tip interacting with the sample be comprised of multiple harmonics of the drive frequency so that the tip displacement, velocity, and acceleration are (with $\theta = \omega_{dr}t - \phi_1$):

$$q(t) = A_0 + \sum_{n=1}^{N} A_n \cos(n\omega_{dr}t - \phi_n)$$

= $A_0 + \sum_{n=1}^{N} A_n \cos(n\theta + n\phi_1 - \phi_n),$ (2a)

$$\frac{dq}{dt} = \dot{q} = -\omega_{dr} \sum_{n=1}^{N} nA_n \sin(n\theta + n\phi_1 - \phi_n), \qquad (2b)$$

$$\frac{d^{2}q}{dt^{2}} = \ddot{q} = -\omega_{dr}^{2} \sum_{n=1}^{N} n^{2} A_{n} \cos(n\theta + n\phi_{1} - \phi_{n}), \qquad (2c)$$

Since the tip motion is assumed to be periodic, so too must the tip-sample interaction force (from equation (1b)). This leads to the following Fourier expansion of the tip-sample interaction force in terms of its conservative and dissipative components:

$$F_{ts}(Z+q(\theta),\dot{q}(\theta)) = F_{ts,CONS}^{0} + F_{ts,CONS}^{1}\cos(\theta)$$

$$+ F_{ts,DISS}^{1}\sin(\theta) + F_{ts,CONS}^{2}\cos(2\theta)$$

$$+ F_{ts,DISS}^{2}\sin(2\theta) + F_{ts,CONS}^{3}\cos(3\theta)$$

$$+ F_{ts,DISS}^{3}\sin(3\theta) + \dots \tag{3}$$

where,

$$F_{ts,CONS}^{0} = \frac{1}{2\pi} \int_{0}^{2\pi} F_{ts} d\theta, \qquad (4a)$$

$$F_{ts,CONS}^{n} = \frac{1}{\pi} \int_{0}^{2\pi} F_{ts} \cos n\theta \ d\theta, \tag{4b}$$

$$F_{ts,DISS}^{n} = \frac{1}{\pi} \int_{0}^{2\pi} F_{ts} \sin n\theta \ d\theta. \tag{4c}$$

In the intermittent contact regime as well as while oscillating in permanent contact, it can be shown that $F_{ts,CONS}(\theta)$ is symmetric about $\theta = \pi$ while $F_{ts,DISS}(\theta)$ is antisymmetric about $\theta = \pi$ [48]. As a result while $F_{ts,CONS}^n$ is the nth Fourier cosine coefficient, $F_{ts,DISS}^n$ is the nth Fourier sine coefficient since $\cos(n\theta)$ and $\sin(n\theta)$ are symmetric and antisymmetric respectively about $\theta = \pi$.

Substituting equations (2) and (3) into equation (1a) and balancing separately the constant, and the cosine and sine harmonic terms in the equation, readily leads to the following results that link the Fourier components of the interaction force to the multi-harmonic microcantilever vibration observables such as harmonic amplitudes and phases. Denoting $r = \frac{\omega_{dr}}{\omega_{far}}$, the *n*th Fourier coefficients of the conservative and dissipative components of the interaction force can be evaluated to be:

$$F_{ts,CONS}^0 = k_{far} A_0, (5a)$$

$$F_{ts,CONS}^{1} = -F_{dr}\cos(\phi_1) + k_{far}A_1(1-r^2),$$
 (5b)

$$F_{ts,DISS}^{1} = F_{dr}\sin(\phi_1) - k_{far}A_1 \frac{r}{Q_{far}},$$
 (5c)

$$F_{ts,CONS}^{2} = k_{far} A_{2} \left[\cos(2\phi_{1} - \phi_{2}) \left(1 - 4r^{2} \right) - \frac{2r}{O_{far}} \sin(2\phi_{1} - \phi_{2}) \right], \tag{5d}$$

$$F_{ts,DISS}^{2} = k_{far}A_{2} \left[-\sin(2\phi_{1} - \phi_{2}) \left(1 - 4r^{2}\right) - \frac{2r}{Q_{far}}\cos(2\phi_{1} - \phi_{2}) \right], \tag{5e}$$

$$F_{ts,CONS}^{3} = k_{far} A_{3} \left[\cos(3\phi_{1} - \phi_{3}) \left(1 - 9r^{2} \right) - \frac{3r}{Q_{far}} \sin(3\phi_{1} - \phi_{3}) \right], \tag{5f}$$

$$F_{ts,DISS}^{3} = k_{far}A_{3} \left[-\sin(3\phi_{1} - \phi_{3}) \left(1 - 9r^{2}\right) - \frac{3r}{Q_{far}}\cos(3\phi_{1} - \phi_{3}) \right].$$
 (5g)

When ω_{dr} is tuned to exact resonance (i.e. $\omega_{dr} = \omega_{far}$ or r=1) with a steady state amplitude $A_{1,far}$, the tip motion $q_{far}(t)$ in the driven eigenmode, the phase lag of tip oscillation relative to the excitation $\phi_{1,far}$, and the magnitude of the driving force F_{dr} are given by:

$$q_{far}(t) = A_{1,far}\cos(\omega_{dr}t - \phi_{1,far}), \quad \phi_{1,far} = \frac{\pi}{2}, \quad F_{dr} = \frac{k_{far}A_{1,far}}{Q_{far}}$$

and equation (5) reduces to

$$F_{ts,CONS}^0 = k_{far} A_0, (6a)$$

$$F_{ts,CONS}^{1} = -\frac{k_{far}A_{1,far}}{Q_{far}}\cos(\phi_{1}), \tag{6b}$$

$$F_{ts,DISS}^{1} = \frac{k_{far}A_{1,far}}{Q_{far}} \left(\sin(\phi_1) - \frac{A_1}{A_{1,far}} \right), \tag{6c}$$

$$F_{ts,CONS}^{2} = k_{far}A_{2} \left[-3\cos(2\phi_{1} - \phi_{2}) - \frac{2}{Q_{far}}\sin(2\phi_{1} - \phi_{2}) \right], \tag{6d}$$

$$F_{ts,DISS}^{2} = k_{far} A_{2} \left[3\sin(2\phi_{1} - \phi_{2}) - \frac{2}{Q_{far}} \cos(2\phi_{1} - \phi_{2}) \right], \tag{6e}$$

$$F_{ts,CONS}^{3} = k_{far} A_{3} \left[-8\cos(3\phi_{1} - \phi_{3}) - \frac{3}{Q_{far}} \sin(3\phi_{1} - \phi_{3}) \right], \tag{6}f$$

$$F_{ts,DISS}^{3} = k_{far} A_{3} \left[8 \sin(3\phi_{1} - \phi_{3}) - \frac{3}{Q_{far}} \cos(3\phi_{1} - \phi_{3}) \right].$$
 (6g)

Equation (6) allows us to extract quantitatively the Fourier harmonics of the conservative and dissipative components of the interaction force in terms of experimental multi-harmonic observables A_0 , A_1 , ϕ_1 , A_2 , ϕ_2 , A_3 , ϕ_3 . The only assumption made so far is that of periodic tip motion and that the tip dynamics is represented by a single-degree-of-freedom model (given by equation (1)).

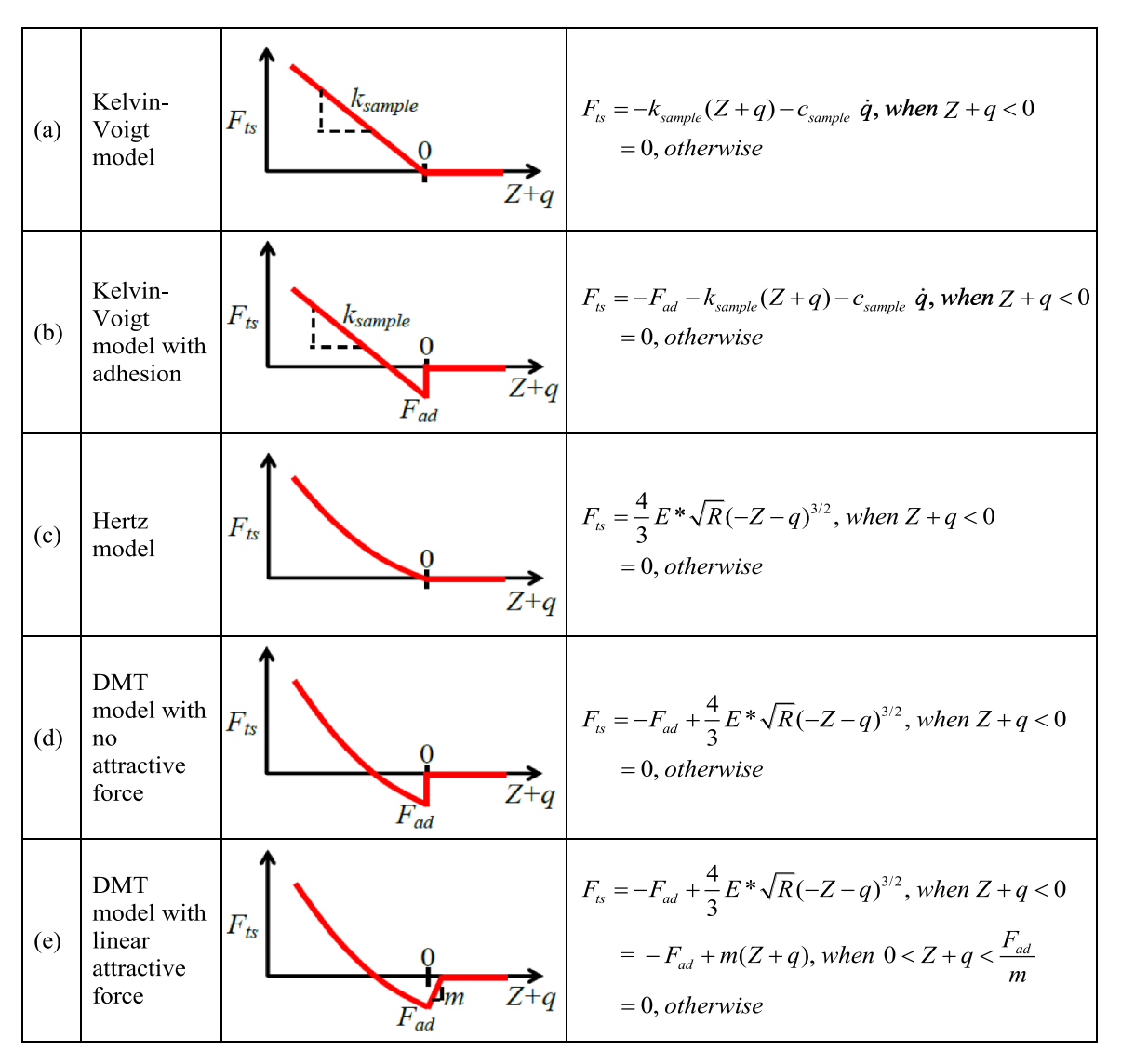


Figure 2. A schematic diagram of the tip-sample interaction force models considered in this work. The force harmonic expressions are derived in terms of material properties for each of these five interaction force models using the multi-harmonic theory developed.

Equation (6) also provides some fundamental insight into the meaning of higher harmonic phase. Specifically, from equations (6c-6g) if the interaction forces are purely conservative, i.e. when $F_{ts.DISS}^n = 0$ we have

first harmonic phase. In particular when $Q_{far} >> 1$, a condition usually met in ambient and vacuum situations, we show in the supplementary material that the following relations hold for

Attractive regime $(\phi_1 > \pi/2)$:

Repulsive regime $(\phi_1 < \pi/2)$:

$$\sin\left(\phi_{1}\right) = \left(\frac{A_{1}}{A_{1,far}}\right),\tag{7a}$$

$$2\phi_1 - \phi_2 \approx 0, \tag{8a}$$

$$\sin(2\phi_1 - \phi_2) = \left(\frac{2}{3Q_{far}}\right)\cos(2\phi_1 - \phi_2),$$
 (7b)

$$3\phi_1 - \phi_3 \approx \pi,\tag{8b}$$

$$\sin(3\phi_1 - \phi_3) = \left(\frac{3}{8Q_{far}}\right)\cos(3\phi_1 - \phi_3). \quad (7c)$$

$$2\phi_1 - \phi_2 \approx \pi,\tag{9a}$$

Equation (7a) is a well-known result in AM-AFM [49]. Equations (7b) and (7c) state that for purely conservative forces the higher harmonic phases are directly related to the

$$3\phi_1 - \phi_3 \approx 0. \tag{9b}$$

The validity of equations (6) is confirmed by comparing with direct simulations of cantilever dynamics on a sample performed with the Virtual Environment for Dynamic AFM (VEDA) [50–52]. These are presented in the following sections.

2.2. Relationship between tip-sample force harmonics and local material properties

The multi-harmonic AFM user needs to choose an appropriate model (figure 2) for the tip-sample interaction in order to convert the measured force harmonics into quantitative nanomechanical properties. In connecting the extracted force harmonics to quantitative nanomechanical properties we use the following approximation

$$q(\theta) \approx A_0 + A_1 \cos \theta,$$
 (10a)

$$\dot{q}(\theta) \approx -A_1 \omega_{dr} \sin \theta,$$
 (10b)

where A_1 is the set-point amplitude during the AM-AFM scan. At first glance this approximation may seem to contradict equation (2). However, equation (10) implies that the 0th and 1st harmonics of the tip motion are sufficient to approximate the interaction force harmonics since these harmonics dominate the tip motion spectrum. The 2nd and 3rd harmonics of tip motion are much smaller in magnitude, so this can be considered a first order approximation relating tip motion to the force harmonics.

A direct consequence of the approximation (equation (10)), is that the maximum penetration of the tip into the sample in an oscillation cycle occurs at $\theta = \pi$ when $q = A_0 - A_1$. Thus, the maximum indentation into the sample $\delta_{\text{max}} = -(Z + q(\theta = \pi))$ during a cycle of oscillation is given by

$$\delta_{\text{max}} = A_1 - Z - A_0, \tag{11}$$

which can be non-dimensionalized by defining

$$\Delta = \frac{\delta_{\text{max}}}{2A_1}.\tag{12}$$

Thus, when $0 < \Delta < 1$ the tip is intermittently tapping on the sample and $\Delta = 1$ implies continuous contact with the sample during the tip oscillation cycle. In terms of equations (10), (11) and (12), the instantaneous tip-sample separation is given by

$$d = Z + q,$$

$$= Z + A_0 + A_1 \cos \theta = -\delta_{\text{max}} + A_1 (1 + \cos \theta),$$

$$= A_1 (-2\Delta + 1 + \cos \theta).$$
(13)

Equation (13) also helps identify that the range of θ over which d < 0 and the tip is in contact with the sample during the oscillation cycle is when $-2\Delta + 1 + \cos\theta < 0$. This requirement can be transformed into the following range of θ for tipsample contact between 0 and 2π :

$$\pi - \cos^{-1}(1 - 2\Delta) < \theta < \pi + \cos^{-1}(1 - 2\Delta).$$
 (14)

In what follows, we show that the approximations (equations (10–11)) lead to analytical/semi-analytical formulas linking material properties to multiple force harmonics for different contact mechanics models shown in figure 2. These formulas are derived by evaluating the integrals given by equations (4) using MAPLE and will be referred to as the tip-indentation formulas from here onwards. Note that the tip-indentation formulas corresponding to DMT model with linear non-contact attractive force (figure 2(e)) are presented in the main article while those for the other models are detailed in the Supplementary Material.

DMT model. The tip sample interaction force modeled with DMT contact mechanics including van der Waals attractive forces and without any dissipation is given by

$$F_{ts} = \begin{cases} -\frac{HR}{6a_0^2} + \frac{4}{3}E^*\sqrt{R}(-Z - q)^{3/2}, & \text{when } Z + q < 0, \\ -\frac{HR}{6(Z + q + a_0)^2}, & \text{otherwise,} \end{cases}$$
(15)

where H is the Hamaker constant, R is the tip radius, a_0 is the intermolecular distance and E^* is the effective Young's modulus for the tip-sample system given in terms of the moduli and Poisson's ratios of the tip and the sample by equation (16).

$$\frac{1}{E^*} = \frac{1 - \nu_{tip}^2}{E_{tip}} + \frac{1 - \nu_{sample}^2}{E_{sample}}.$$
 (16)

Evaluation of the integrals (equations (4)) with the attractive van der Waals force term when Z+q>0 (equation (15)) did not lead to closed form expressions for the tip-indentation formulas using MAPLE. Therefore, we approximate this with a linear attractive force which is discussed in detail below. An alternative approximation where the non-contact attractive term is neglected is presented in the Supplementary Material.

DMT model with linear non-contact attractive force. A schematic of the DMT model with linear non-contact attractive force is as shown in figure 2(e) and is given by

$$F_{ts} = \begin{cases} -F_{ad} + \frac{4}{3}E^*\sqrt{R}(-Z - q)^{3/2}, & \text{when } Z + q < 0, \\ -F_{ad} + m(Z + q), & \text{when } 0 < Z + q < \frac{F_{ad}}{m}, \\ 0, & \text{otherwise,} \end{cases}$$
(17)

where F_{ad} is the force of adhesion and m represents the slope of the linear attractive part of the interaction force. Introducing $\Lambda = \frac{4}{3}E^*\sqrt{R}, \gamma = \frac{F_{ad}}{\Lambda(A_1)^{3/2}}$ and $\beta = \frac{m}{\Lambda(A_1)^{1/2}}$, the range of θ over which Z+q or $d<\frac{F_{ad}}{m}$ during the oscillation cycle, i.e. when $-2\Delta+1+\cos\theta<\frac{\gamma}{\beta}$ can be identified as

$$\pi - \cos^{-1}\left(1 - 2\Delta - \frac{\gamma}{\beta}\right) < \theta < \pi + \cos^{-1}\left(1 - 2\Delta - \frac{\gamma}{\beta}\right). \tag{18}$$

Substituting equations (13) and (17) into equations (4) and evaluating the integrals based on the limits on θ specified

by equations (14) and (18), the tip-indentation formulas corresponding to this tip-sample interaction force in Δ can be determined exactly using MAPLE as:

$$F_{ts,CONS}^{0} = \frac{1}{\pi} \Lambda A_{1}^{(3/2)} \gamma \left(\bar{\theta}_{2} - \pi \right) + \frac{4\sqrt{2}}{3\pi} \Lambda A_{1}^{(3/2)} \begin{pmatrix} \Delta_{EK} (3\Delta^{2} - 5\Delta + 2) \\ + \Delta_{EE} (4\Delta - 2) \end{pmatrix} + \frac{\beta}{\pi} \Lambda A_{1}^{(3/2)} \begin{pmatrix} (2\Delta - 1) \left(\bar{\theta}_{2} - \bar{\theta}_{1} \right) \\ + 2\sqrt{\Delta} \sqrt{1 - \Delta} - \alpha \end{pmatrix}, \quad (19a)$$

$$\begin{split} F_{ts,CONS}^{1} &= \frac{1}{\pi} \Lambda A_{1}^{(3/2)} \gamma \alpha \\ &+ \frac{8\sqrt{2}}{5\pi} \Lambda A_{1}^{(3/2)} \left(\begin{array}{c} \Delta_{EK} (\Delta^{2} - 3\Delta + 2) \\ + \Delta_{EE} (-2\Delta^{2} + 2\Delta - 2) \end{array} \right) \\ &+ \frac{\beta}{\pi} \Lambda A_{1}^{(3/2)} \left(\begin{array}{c} \bar{\theta_{1}} - \bar{\theta_{2}} \\ + (1 - 2\Delta) \left(2\sqrt{\Delta}\sqrt{1 - \Delta} - \alpha \right) \end{array} \right), \end{split}$$

$$\begin{split} F_{\rm IS,CONS}^2 &= \frac{4}{3\pi} \Lambda A_1^{(3/2)} \gamma \left(2\Delta - 1 + \frac{\gamma}{\beta} \right) \alpha \\ &+ \frac{8\sqrt{2}}{35\pi} \Lambda A_1^{(3/2)} \left(\begin{array}{c} \Delta_{EK} (8\Delta^3 - 13\Delta^2 + 3\Delta + 2) \\ + \Delta_{EE} (-16\Delta^3 + 24\Delta^2 - 4\Delta - 2) \end{array} \right) \\ &+ \frac{8}{3\pi} \Lambda A_1^{(3/2)} \beta \Delta (1 - \Delta) \left(2\sqrt{\Delta} \sqrt{1 - \Delta} - \alpha \right), \end{split} \tag{19c}$$

$$\begin{split} F_{is,CONS}^{3} &= \frac{2}{3\pi} \Lambda A_{1}^{(3/2)} \gamma \left(2 + 12\Delta(\Delta - 1) + 3(2\Delta - 1) \frac{\gamma}{\beta} + \frac{\gamma^{2}}{\beta^{2}} \right) \alpha \\ &+ \frac{8\sqrt{2}}{315\pi} \Lambda A_{1}^{(3/2)} \begin{pmatrix} \Delta_{EK} \left(\begin{array}{c} 128\Delta^{4} - 272\Delta^{3} \\ +159\Delta^{2} - 13\Delta - 2 \end{array} \right) \\ +\Delta_{EE} \left(\begin{array}{c} -256\Delta^{4} + 512\Delta^{3} \\ -270\Delta^{2} + 14\Delta + 2 \end{array} \right) \end{pmatrix} \\ &+ \frac{8}{3\pi} \Lambda A_{1}^{(3/2)} \beta \Delta (-2\Delta^{2} + 3\Delta - 1) \left(2\sqrt{\Delta}\sqrt{1 - \Delta} - \alpha \right), \end{split}$$

where $\bar{\theta}_1 = \cos^{-1}(2\Delta - 1)$, $\bar{\theta}_2 = \cos^{-1}\left(2\Delta - 1 + \frac{\gamma}{\beta}\right)$, Δ_{EK} and Δ_{EE} are the elliptic integrals, $EllipticK\left(\sqrt{\Delta}\right)$ and $EllipticE\left(\sqrt{\Delta}\right)$ respectively and $\alpha = \sqrt{4\Delta(1-\Delta)-2(2\Delta-1)\frac{\gamma}{\beta}-\frac{\gamma^2}{\beta^2}}$. Note that the dissipative force harmonics will be zero here as the model for tip-sample interactions does not include any dissipation. An equivalence between this model (equation (17)) and the original DMT model (equation (15)) is established by equating the areas under the non-contact attractive parts of the interaction force models given by equations (15) and (17) which resulted in a simple relation $m = \frac{F_{adl}}{2a_0}$ under the assumption $a_0 << A_1$. This assumption is reasonable especially for the AFM studies in ambient conditions or under vacuum as a_0 is of the order of 0.1 nm whereas A_1 is of the order of tens of nanometers.

3. Simulations

For computational validation, we perform simulations using Virtual Environment for Dynamic Atomic Force Microscopy (VEDA) [50–52], a tool available on nanohub.org for AFM simulations. A probe, typically used for AM-AFM, with properties of $k_{far}=26$ N/m, $\omega_{far}=303$ kHz, $Q_{far}=456$, R=10 nm was used in the simulations with the excitation frequency equaling its fundamental resonance frequency $\omega_{far}=303$ kHz resulting in $A_{1,far}=85$ nm. The dynamic approach curves are simulated in VEDA on a sample with $E_{sample}=1$ GPa by assuming DMT contact [53] with $F_{ad}=20$ nN.

3.1. Validation of equations (6)

The process to check the validity of the relations (equations (6)) connecting the multi-harmonic observables and force harmonics is shown schematically in figure 3. The input simulation parameters such as k_{far} , $A_{1,far}$, Q_{far} and the output parameters from simulation like A_0 , A_1 , ϕ_1 , A_2 , ϕ_2 are used to calculate the conservative force harmonics using equations (6). The force harmonics amplitudes obtained up to the 2nd harmonic calculated using equations (6) match closely with those from direct numerical simulations (error < 5%) over a wide range of amplitude set-point ratios (figure 4). This comparison of force harmonics has been performed with a number of simulations by varying E_{sample} from 0.01 GPa to 10 GPa, F_{ad} from 0 nN to 50 nN, $A_{1,far}$ from 50 nm to 100 nm and k_{far} from 0.5 N/m to 40 N/m. For all these simulations, the force harmonics calculated using equations (6), match very well with those from direct VEDA simulations over a wide range of set-point ratios (0.2-0.9).

3.2. Validation of equations (19)

The relations given by equations (19) connecting the force harmonics to indentation and local material properties are validated using the data from the same VEDA simulations discussed in section 3. Note that VEDA incorporates original DMT model (equation (15)) in the simulation. A schematic illustration of the validation process is shown in figure 5. The input simulation parameters E_{sample} , ν_{sample} , E_{tip} , ν_{tip} , F_{ad} , R, a_0 and the output parameters A_1 , δ_{max} are used to calculate the conservative force harmonics using the tip-indentation formulas (equations (19)). A comparison of their amplitudes with those computed directly from numerical simulations in figure 6, shows excellent agreement (within 5%) over setpoint ratios ranging from 0.15-0.9. This comparison is also performed with numerous simulations performed by varying E_{sample} , F_{ad} , $A_{1,far}$ and k_{far} in the same ranges as were chosen earlier in section 3.1. The following remarks are drawn based on those comparisons:

a. The force harmonics from tip-indentation formulas are within 10% to those obtained directly from simulations over a large range (0.3–0.85) of set-point ratios but start to deviate outside this range.

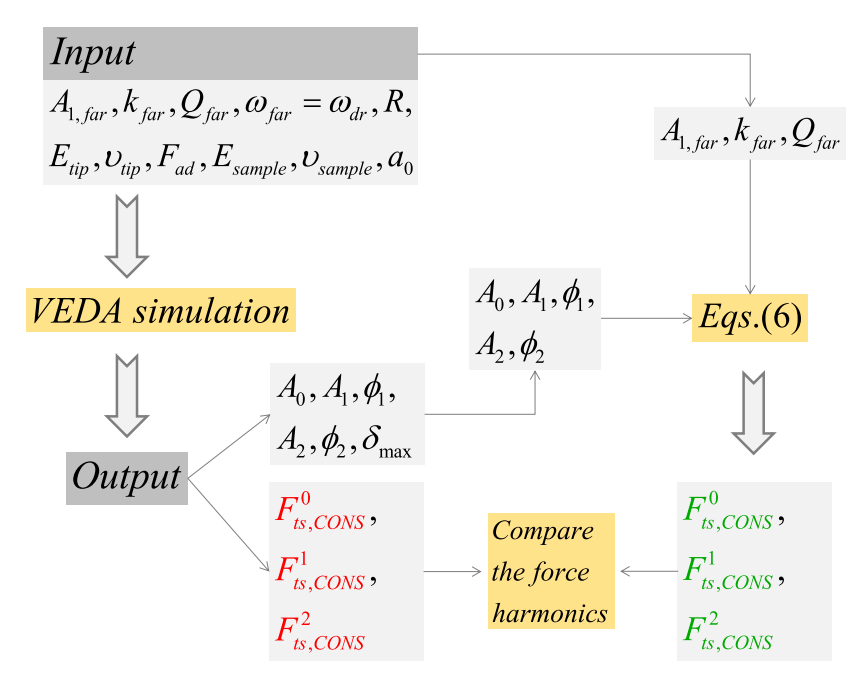


Figure 3. A flow chart illustrating the validation process of derived force harmonics in terms of observables (equations (6)). The input simulation parameters $A_{1,far}$, k_{far} , Q_{far} and output parameters A_0 , A_1 , ϕ_1 , A_2 , ϕ_2 are fed through equations (6) to obtain the force harmonics which need to be compared to those obtained directly from VEDA output to check their validity.

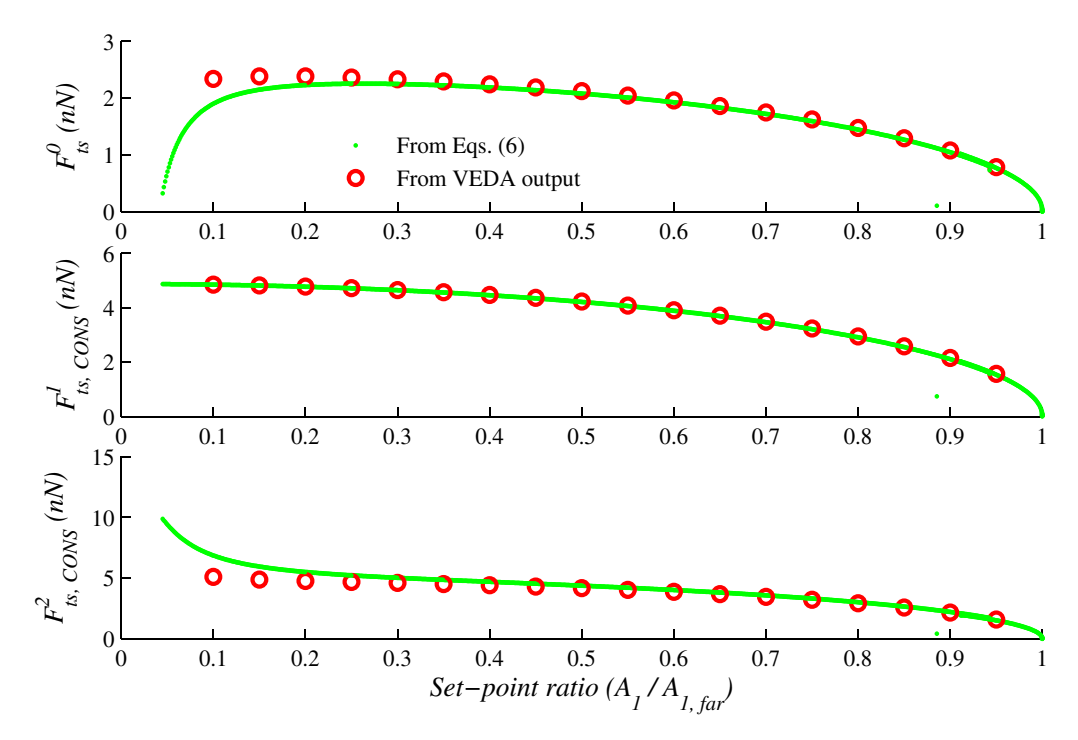


Figure 4. A comparison of the conservative force harmonic amplitudes obtained from microcantilever observables and those obtained from direct numerical simulations in VEDA shows good match. The simulation is done with a probe of $k_{far} = 26$ N/m, $\omega_{far} = 303$ kHz, $Q_{far} = 456$, R = 10 nm by driving it such that $\omega_{dr} = \omega_{far}$ with $A_{1,far} = 85$ nm. The dynamic approach curves are simulated on a sample with $E_{sample} = 1$ GPa by assuming DMT contact (equation (15)) with $F_{ad} = 20$ nN. Note that the green outlier data at a set-point ratio of ≈ 0.9 is due to the resulting transients while the microcantilever jumps from the attractive to the repulsive regime. This can be avoided in simulations by choosing a slow approach speed of the microcantilever towards the sample.

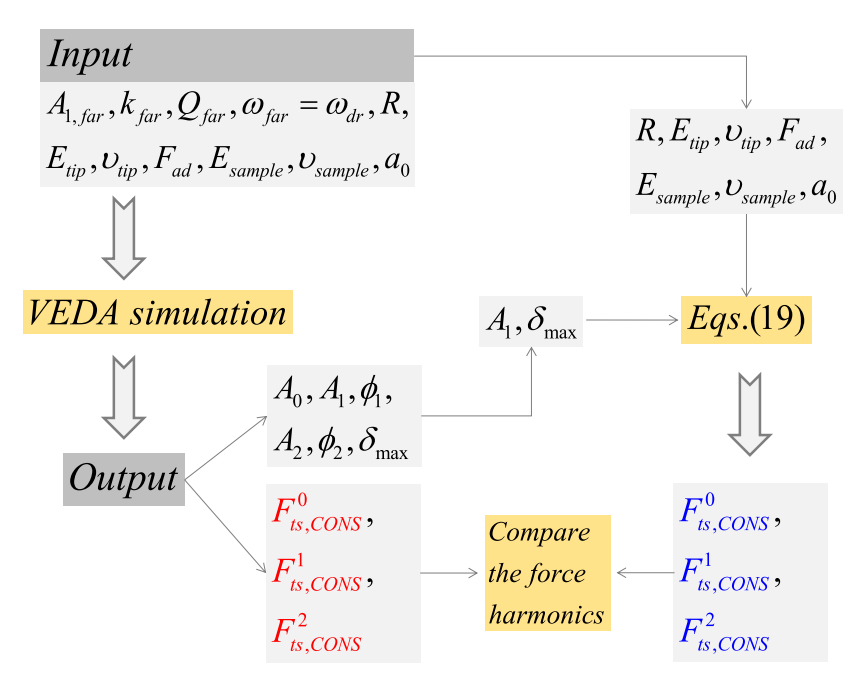


Figure 5. A flow chart illustrating the validation process of derived force harmonics in terms of material properties (equations (19)). The input simulation parameters R, E_{tip} , ν_{tip} , F_{ad} , E_{sample} , ν_{sample} , a_0 and output parameters A_1 , δ_{max} are fed through equations (19) to obtain the force harmonics which need to be compared to those obtained directly from VEDA output to check their validity.

b. This deviation becomes larger with increasing F_{ad} , especially for combinations of higher F_{ad} and lower E_{sample} and k_{far} values. The reasons for this deviation could be the approximation given by equation (10) and the simplification of the van der Waals non-contact attractive force in the original DMT model with a linear approximation. Also, note that the use of any classical contact mechanics model like DMT to describe contact between a hard and soft material is at best an approximation, especially whenever deformations are large. A better approach might require a model better designed to describe contact between a hard and soft material [54], or more recent approaches based on the use of Attard's model [55, 56].

3.3. Method to estimate material properties

The theory described above allows the estimation of local nanoscale properties of the sample in a two step process. First a small subset of multi-harmonic microcantilever observables, the amplitudes and phases of the 0th, 1st and 2nd, or the 1st, 2nd and 3rd are acquired during a regular tapping mode/AM-AFM scan. These are converted to an equal number of conservative and dissipative force harmonics using equations (6). Finally the unknown local physical properties in a chosen tip-sample contact mechanics model are fit so that the force harmonics using the tip-indentation formulas (equations (19)) match the experimental force harmonics (equations (6)) in a least square sense. For example, the unknown material properties in the DMT model are the sample modulus (E_{sample}), force of adhesion (F_{ad}) and maximum indentation (δ_{max}) . Therefore we just need any three force harmonics to extract these three properties. In the present work, the 0th, 1st and 2nd conservative force harmonics for the DMT contact model given by equations (19a, b, c) are used to extract these three properties, although the method can be easily extended to the 1st, 2nd and 3rd harmonic as well.

First, we demonstrate this property estimation approach using VEDA simulations. We used the same microcantilever properties and observables A_0, A_1, ϕ_1, A_2 and ϕ_2 from the simulation in section 3 to obtain the 0th, 1st and 2nd conservative force harmonics using equation (6). The obtained force harmonics are fit to the tip-indentation formulas for the DMT model with linear attractive force given by equations (19a, b, c) using non-linear least squares to extract the material properties. We used a parameter, N_r to check the goodness of these fits and the estimated properties based on this approach are shown in figure 7. As can be seen, the estimated properties match the properties used in the simulation within 10% over a wide range of set-point ratios with N_r value being smaller than 0.1. The definition of N_r as well as the details of the non-linear least square fitting process are discussed in the supplementary material.

4. Experiments

The multi-harmonic approach is demonstrated with experiments performed on a Cypher AFM in amplitude modulated mode under ambient conditions. We used the highly doped silicon PPP-NCLR probes from Nanosensors that have a stiffness in the range of 21–98 N/m and fundamental resonance frequency of 146–236 kHz. The sample used in this work is a blend of Polystyrene and Polyolefin elastomer (ethylene-octene copolymer) or simply referred to as PS-LDPE [45], from Bruker AFM probes.

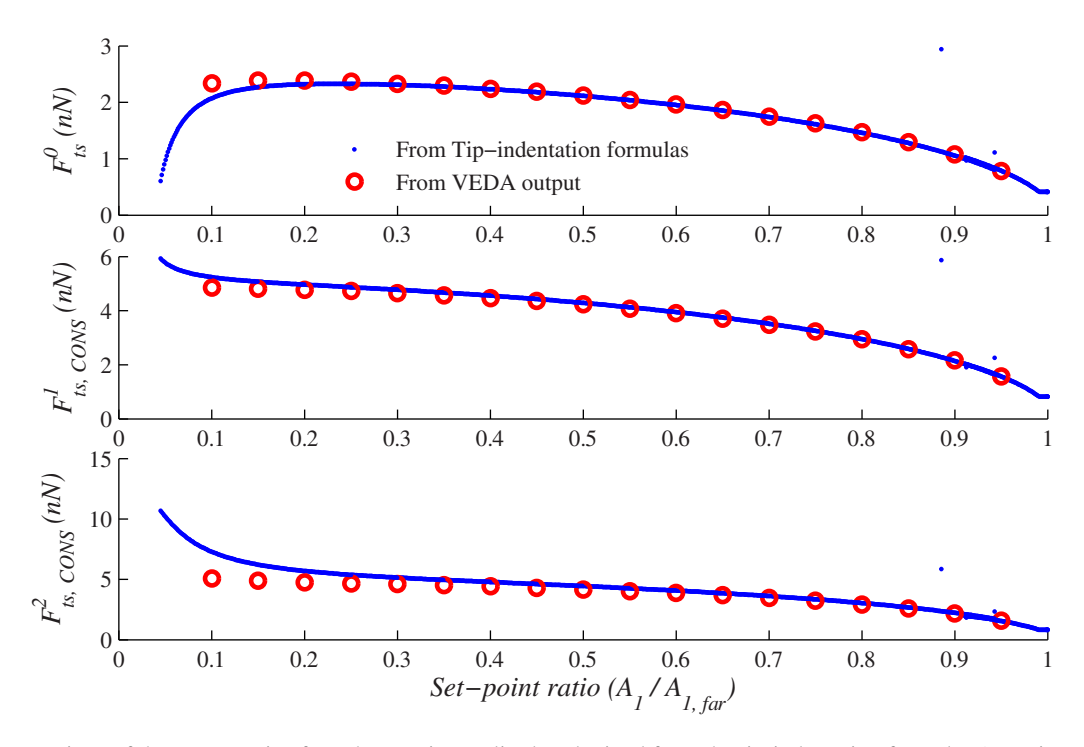


Figure 6. A comparison of the conservative force harmonic amplitudes obtained from the tip-indentation formulas (equations (19)) and those obtained from direct numerical simulations in VEDA shows good agreement over a wide range of set-point ratio. The simulation is done with a probe of $k_{far} = 26$ N/m, $\omega_{far} = 303$ kHz, $Q_{far} = 456$, R = 10 nm by driving it such that $\omega_{dr} = \omega_{far}$ with $A_{1,far} = 85$ nm. The dynamic approach curves are simulated on a sample with $E_{sample} = 1$ GPa by assuming DMT contact (equation (15)) with $F_{ad} = 20$ nN. The values of E_{tip} , ν_{tip} , ν_{sample} , a_0 used in the simulation are 130 GPa, 0.3, 0.3, 0.2 nm respectively. Note that the blue outlier data at around a set-point ratio of 0.9 is due to the resulting transients while the microcantilever jumps from the attractive to the repulsive regime. This can be avoided in simulations by choosing a slow approach speed of the microcantilever towards the sample.

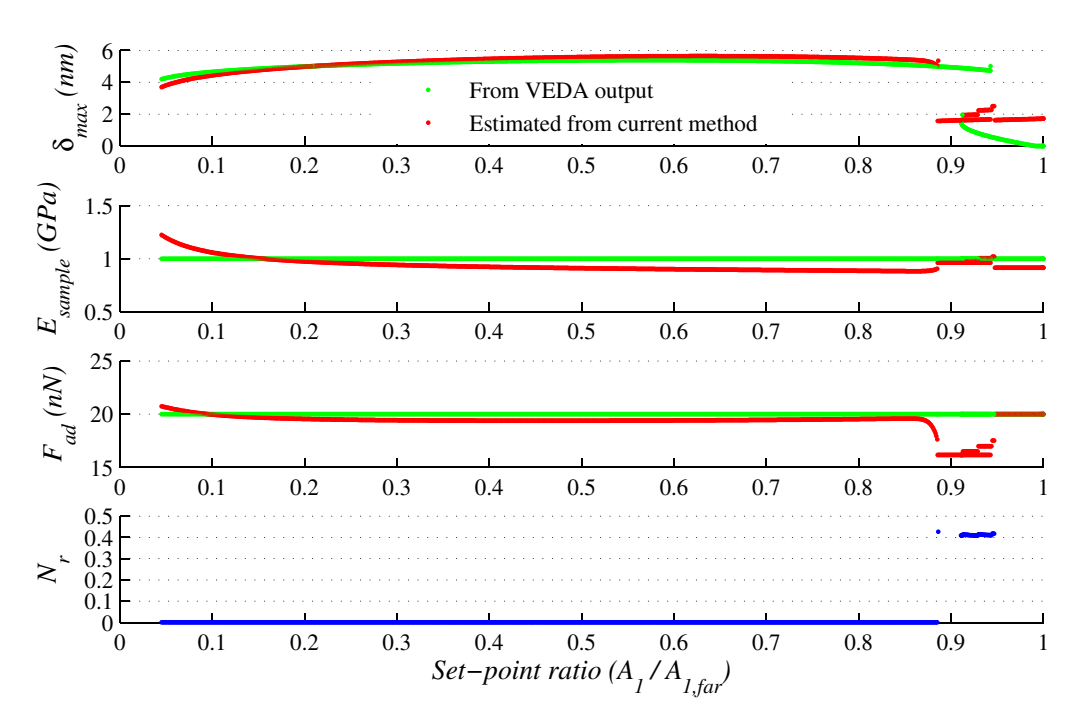


Figure 7. The predicted properties for the simulated data using the proposed multi-harmonic property estimation approach. The estimated properties from the current method are within 10% of the actual properties used in the simulation over a wide range of set-point ratios. The simulation is done with a probe of $k_{far} = 26 \text{ N/m}$, $\omega_{far} = 303 \text{ kHz}$, $Q_{far} = 456$, R = 10 nm by driving it such that $\omega_{dr} = \omega_{far}$ with $A_{1,far} = 85 \text{ nm}$. The dynamic approach curves are simulated on a sample with $E_{sample} = 1 \text{ GPa}$ by assuming DMT contact (equation (15)) with $F_{ad} = 20 \text{ nN}$. Note that the N_r shown is the metric used to decide the goodness of non-linear least squares fit implemented with the proposed multi-harmonic method. The solution is decided by consistently maintaining N_r below 0.1 over a wide range of set-point ratios.

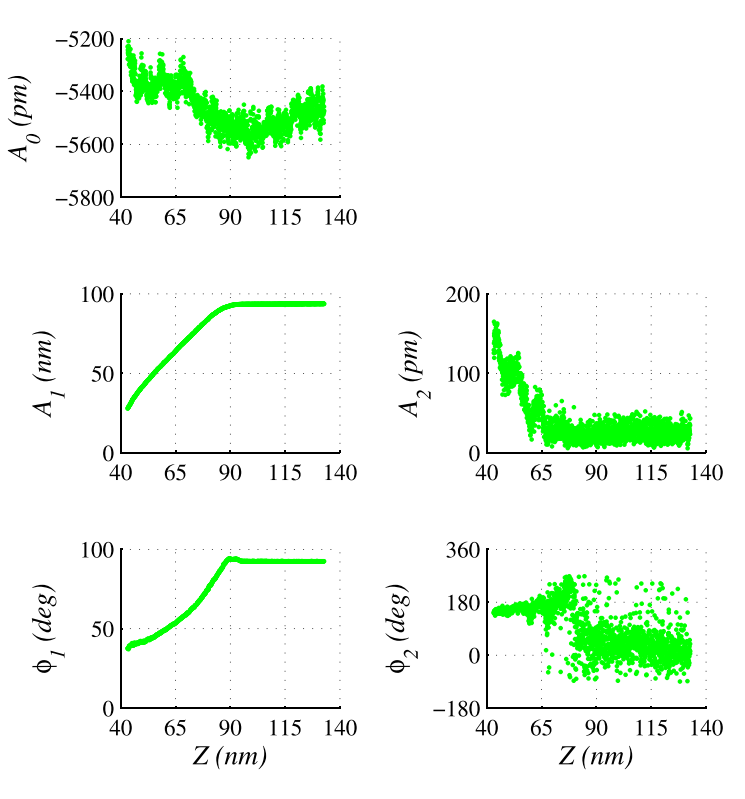


Figure 8. The raw dynamic approach data acquired on the PS region of the PS-LDPE sample plotted against Z. The tip-sample interactions start when Z is about 95 nm (see ϕ_1 plot). Note that the 0th harmonic is not zero prior to the interaction and needs to be adjusted. Similarly the 2nd harmonic amplitude is also non-zero before the interaction begins. This is attributed to the photodiode non-linearity. Also, A_2 appears to be increasing at around Z = 70 nm as opposed to 95 nm. This could be due to the noise on A_2 but ϕ_2 appears to provide a better signature for the onset of higher harmonics. Properties of the microcantilever used for the experiments are $k_{far} = 16.4$ N/m, $\omega_{far} = 161.8$ kHz, $Q_{far} = 287$, R = 10 nm, which is driven at $\omega_{dr} = \omega_{far}$ with $A_{1,far} = 94$ nm.

4.1. Adjustment of experimental observables for instrument nonlinearities and latencies

A set of experimental data was acquired with a microcantilever with calibrated $k_{far} = 16.4$ N/m, $\omega_{far} = 161.8$ kHz and $Q_{far} = 287$. It is driven at its fundamental resonance frequency $\omega_{far} = 161.8$ kHz with $A_{1,far} = 94$ nm and brought closer to the sample gradually while acquiring the observables A_0 , A_1 , ϕ_1 , A_2 and ϕ_2 on the PS region as shown in figure 8 as a function of Z.

In theory, A_0 prior to interaction should vanish but is nonzero in experimental data. The 0th harmonic can slowly drift from zero even after the mean deflection from the microcantilever is zeroed at the start of experiment. This artifact can be removed by subtracting the mean A_0 signal far from sample from the entire A_0 vs. Z data set. Likewise, when far from the sample, A_2 should be zero and ϕ_2 should be undefined. In practice, as seen in figure 8, both these 2nd harmonic observables have a value for large Z far enough for no tip-sample interactions to exist. This artifact is due to electronic and photodiode nonlinearities [57]. Therefore, they are corrected based on a systematic approach presented in detail in the supplementary material. The microcantilever observables obtained after all these corrections are shown in figure 9.

The observables A_1 , ϕ_1 and those corrected $(A_0, A_2 \text{ and } \phi_2)$ were used in conjunction with the tip-indentation formulas for

the DMT model with linear non-contact attractive force given by equations (19) and non-linear least squares to estimate maximum sample indentation, elastic modulus and force of adhesion. The estimated properties on the PS region of the sample while assuming $E_{tip} = 130$ GPa, $\nu_{tip} = 0.3$, $\nu_{sample} = 0.3$, $a_0 = 0.2$ nm and R = 10 nm are shown in figure 10. For set-point ratios under 0.7, the estimated PS elastic modulus is close to the expected value of 2 GPa [45], and the estimated modulus and adhesion remain unchanged. The goodness of non-linear least squares is decided by maintaining N_r below 0.1 for all the experimental results presented here.

4.2. Estimation of properties of PS-LDPE from experimental scans

The multi-harmonic method developed is further applied to maps of PS-LDPE sample acquired at a specific set-point. We acquired the maps of observables with the same microcantilever used under the same experimental conditions presented in section 4.1 at a set-point ratio of 0.42 in the repulsive regime. The 0th and 2nd harmonic maps are adjusted by referring to the corrected approach curves data on PS in the previous section. This is done by matching the 0th and 2nd harmonic data on the PS region of the maps to that on the corrected PS approach curves. These adjustments in the 0th and 2nd harmonic maps on the PS region are assumed to correct those on the LDPE region of the sample. It is reasonable to

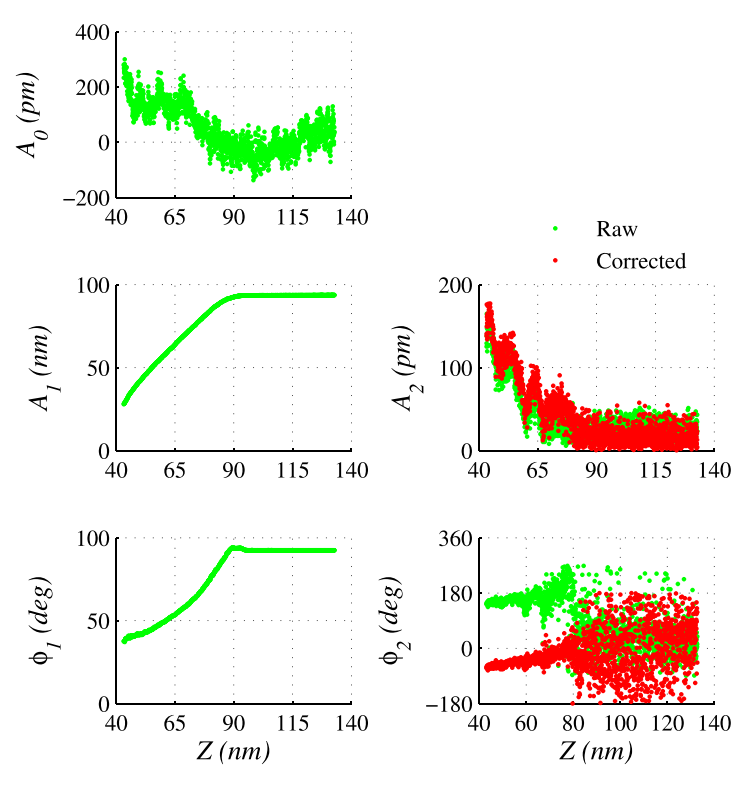


Figure 9. The corrected approach data on the PS region of the sample. The 0th harmonic is shifted such that it is zero before the beginning of tip-sample interaction. The non-linearity in the 2nd harmonic is corrected and the corrected data is shown along with the raw data. Properties of the microcantilever used for the experiments are $k_{far} = 16.4$ N/m, $\omega_{far} = 161.8$ kHz, $Q_{far} = 287$, R = 10 nm, which is driven at $\omega_{dr} = \omega_{far}$ with $A_{1,far} = 94$ nm.

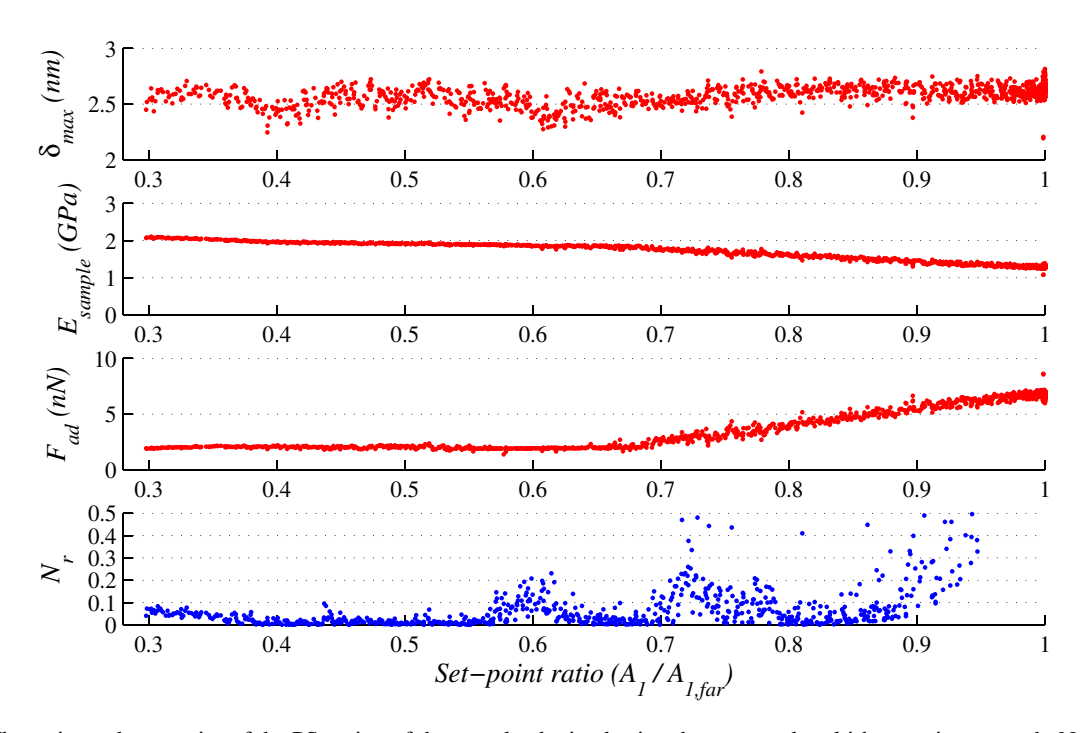


Figure 10. The estimated properties of the PS region of the sample obtained using the proposed multi-harmonic approach. Note that tip-indentation formulas given by equations (19) were used to estimate these properties. The predicted modulus of PS is very close to the expected value of 2 GPa [45] over a large set-point range. Note that N_r is mostly below 0.1 for set-point ratios less than 0.7. The properties of the microcantilever used for the experiments are $k_{far}=16.4$ N/m, $\omega_{far}=161.8$ kHz, $Q_{far}=287$, R=10 nm, which is driven at $\omega_{dr}=\omega_{far}$ with $A_{1,far}=94$ nm.

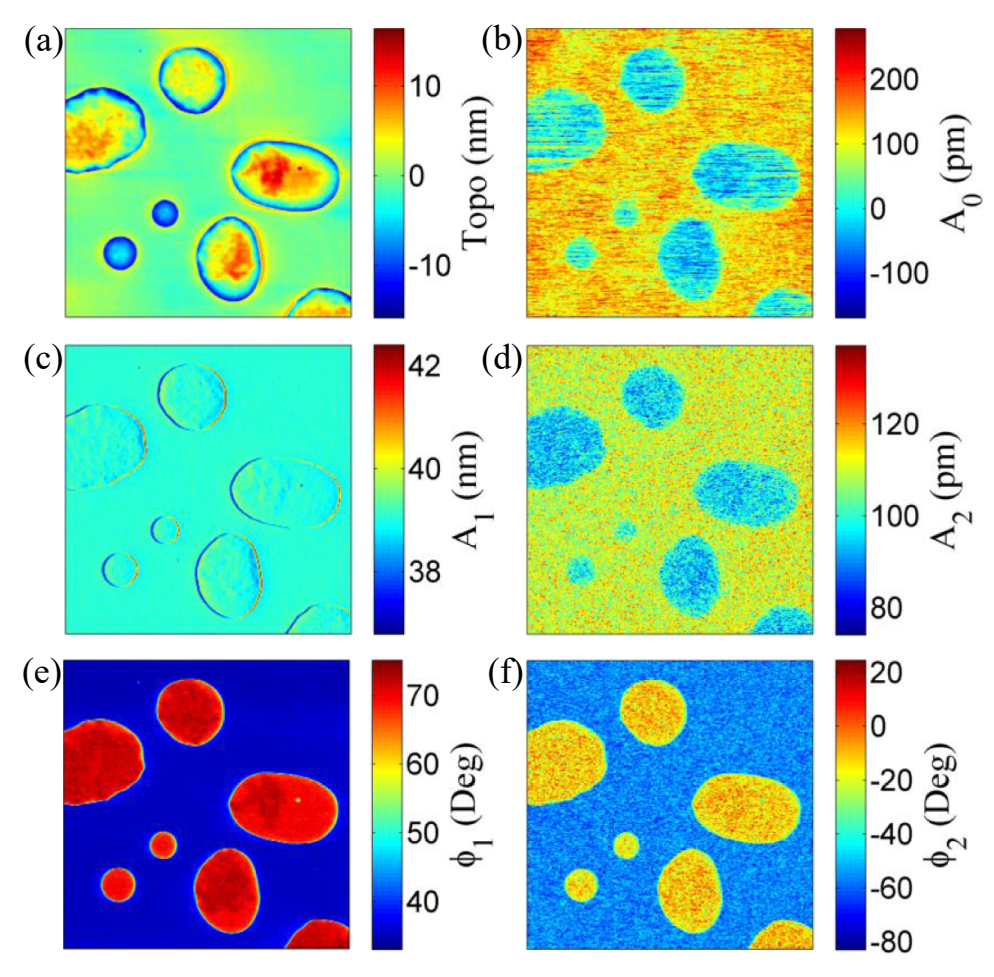


Figure 11. The harmonic observable maps acquired on the PS-LDPE sample at a set-point amplitude of $A_1 = 39.1$ nm. Note that these are the corrected maps based on the correction of 0th and 2nd harmonics of the approach curves data on PS. The properties of the microcantilever used for the experiments are $k_{far} = 16.4$ N/m, $\omega_{far} = 161.8$ kHz, $Q_{far} = 287$, R = 10 nm, which is driven at $\omega_{dr} = \omega_{far}$ with $A_{1.far} = 94$ nm. Note that all the images are of size 8 μ m × 8 μ m, containing 256 × 256 pixels, obtained with a scan rate of 1 Hz.

do so as both the approach curves and the maps are acquired with the same microcantilever operated under same conditions in the same experiment. The corrected maps thus obtained are shown in figure 11. The topography of the sample shown in figure 11(a) consists of circular domains of LDPE distributed over the flat PS matrix. Figures 11(b)–(f) show the maps of microcantilever harmonic observables A_0 , A_1 , A_2 , ϕ_1 and ϕ_2 respectively. Note that the size of these maps is 8 μ m × 8 μ m, consisting of 256 × 256 pixels, acquired with a scan rate of 1 Hz.

The proposed multi-harmonic approach implemented with non-linear least squares is used to estimate the properties of the PS-LDPE sample from these harmonic observable maps and the estimated properties are as shown in figure 12. The estimated maps of maximum indentation, sample modulus and force of adhesion are shown in figure 12(a)–(c) respectively and the corresponding histograms are presented in figures 12(e)–(g). The values of maximum indentation on PS and LDPE are 2.42 \pm 0.07 nm and 17.54 \pm 0.29 nm respectively. The values of sample modulus on PS and LDPE are 1.93 \pm 0.01 GPa and 93.78 \pm 0.86 MPa respectively and the values of adhesion force on PS and LDPE are 1.91 \pm 0.10 nN and 16.24 \pm 0.81

nN respectively. Note that the N_r representing the goodness of non-linear least squares is maintained below 0.1 for more than 90% of the data and is shown in figures 12(d) and (h). Accuracy of the quantitative results for material property mapping presented in this work depends on the validity of the chosen interaction force model for the specific tip-sample interaction combination. The values of sample modulus and indentation measured using the method on the PS-LDPE sample are in fact in close agreement with those reported in [36, 40, 45]. However on the LDPE part of the sample, the estimated value of adhesion is higher than that on PS which is contrary to what was reported in [36, 40]. We attribute this difference to the viscoelasticity of this sample which is absent in the DMT model. Large viscoelasticity can in fact manifest as large values of minimum force during a tip oscillation cycle, which can be mistaken as a large adhesion force. In fact, the extension of the present approach to include viscoelastic dissipation [56] is ongoing work.

The properties are further estimated from the observable maps obtained at multiple set-point ratios (0.31, 0.42 and 0.52) and the corresponding data are presented in figure 13. As can be seen from the figure, the mean values of maximum

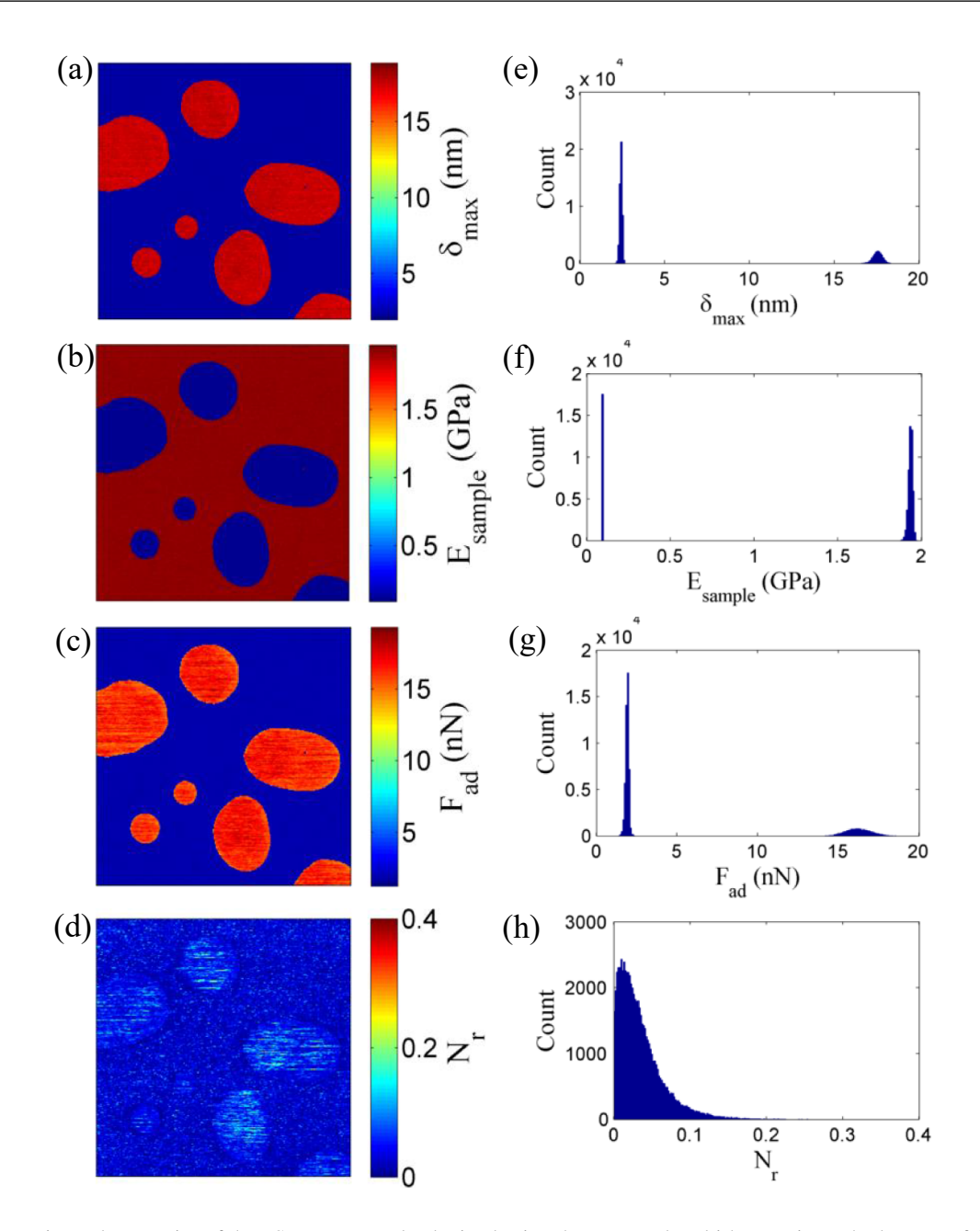


Figure 12. The estimated properties of the PS-LDPE sample obtained using the proposed multi-harmonic method. Maps of (a) maximum indentation (b) sample modulus (c) adhesion force (d) goodness of fit parameter N_r and their respective histograms in (e), (f), (g) and (h). Note that N_r is below 0.1 for more than 90% of the data in the maps and it is below 0.2 for about 99% of the data. The properties of the microcantilever used for the experiments are $k_{far} = 16.4$ N/m, $\omega_{far} = 161.8$ kHz, $Q_{far} = 287$, R = 10 nm, which is driven at $\omega_{dr} = \omega_{far}$ with $A_{1,far} = 94$ nm. All the images are of size 8 μ m × 8 μ m, containing 256 × 256 pixels.

indentation, sample modulus and adhesion force on PS and LDPE are similar to those presented earlier with relatively small standard deviations. An additional data set has been acquired using a different cantilever on the same sample and is presented in the supplementary material.

5. Conclusions

A multi-harmonic AFM method using standard AFM microcantilevers in a tapping mode scan is presented that

relies on using only a few harmonics of the microcantilever deflection to extract the nanomechanical properties of materials is proposed. The method is developed for a variety of tip-sample interactions. The theory associated with the proposed method not only helps us gain important insights into the relationships between the interaction force harmonics, microcantilever deflection harmonics and material properties, but also reveals the dependence of phases of higher harmonics of microcantilever deflection on the first harmonic phase. The analytical/semi-analytical relationships are carefully validated through direct simulations of

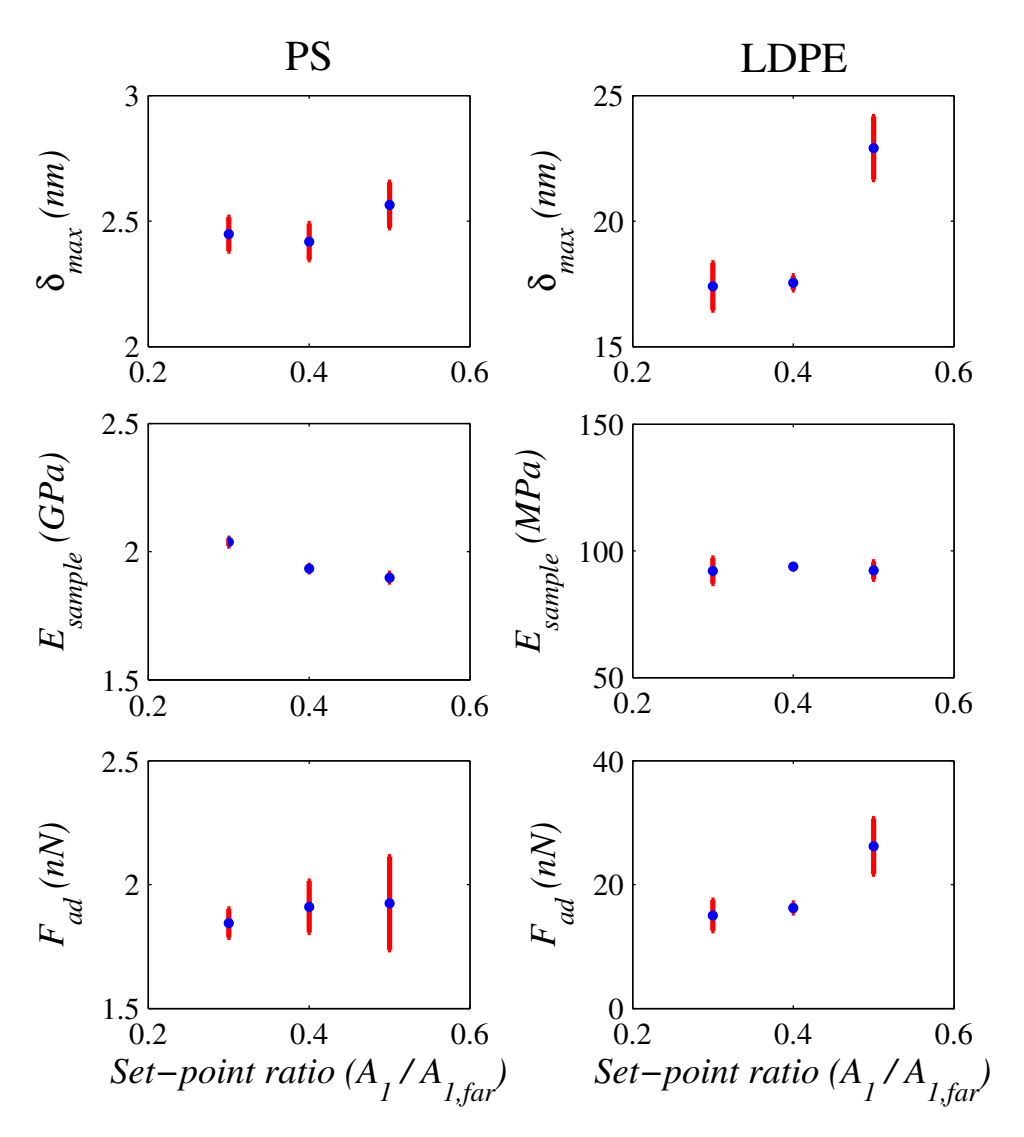


Figure 13. The estimated properties of the PS-LDPE sample obtained at different set-points. The properties of the PS are similar for different set-points considered while the properties of the soft poylemr, LDPE are changing by about 40% depending on the set-point. However, the standard deviation of the estimates is relatively small compared to the mean values.

microcantilever dynamics in VEDA. Experimental validation is performed on a PS-LDPE polymer blend to map the local elastic modulus, indentation and adhesion from a single tapping mode/AM-AFM scan. The approach opens up the possibility of using a small set of multi-harmonic observables during standard tapping mode AM-AFM scans in air/vacuum for quantitative nanomechanical mapping of heterogeneous samples.

Acknowledgments

We would like to thank Dr M. Cadena for inputs on experimental data collection and Dr R. Potekin for helpful comments on the manuscript. We gratefully acknowledge funding for this research from the National Science Foundation under the grant "CMMI1726274, GOALI: Multi-frequency dynamics in the Atomic Force Microscope".

ORCID iD

Arvind Raman https://orcid.org/0000-0001-6297-5581

References

- [1] Garca R and Perez R 2002 Dynamic atomic force microscopy methods Surf. Sci. Rep. 47 197–301
- [2] Giessibl F J 2003 Advances in atomic force microscopy Rev. Mod. Phys. 75 949–83
- [3] Rodrguez T R and Garca R 2004 Compositional mapping of surfaces in atomic force microscopy by excitation of the second normal mode of the microcantilever *Appl. Phys.*Lett. 84 449–51
- [4] Martinez N F, Lozano J R, Herruzo F G E T, Richter C, Sulzbach T and Garcia R 2008 Bimodal atomic force microscopy imaging of isolated antibodies in air and liquids Nanotechnology 19 384011
- [5] Proksch R 2006 Multifrequency, repulsive-mode amplitude-modulated atomic force microscopy *Appl. Phys. Lett.* 89 113121

- [6] Kawai S, Glatzel T, Koch S, Such B, Baratoff A and Meyer E 2009 Systematic achievement of improved atomic-scale contrast via bimodal dynamic force microscopy *Phys. Rev.* Lett. 103 220801
- [7] Martinez N F, Patil S, Lozano J R and Garcia R 2006 Enhanced compositional sensitivity in atomic force microscopy by the excitation of the first two flexural modes Appl. Phys. Lett. 89 153115
- [8] Solares S D and Chawla G 2010 Frequency response of higher cantilever eigenmodes in bimodal and trimodal tapping mode atomic force microscopy *Meas. Sci. Technol.* 21 125502
- [9] Jesse S, Kalinin S V, Proksch R, Baddorf A P and Rodriguez B J 2007 The band excitation method in scanning probe microscopy for rapid mapping of energy dissipation on the nanoscale *Nanotechnology* 18 435503
- [10] Platz D, Tholén E A, Pesen D and Haviland D B 2008 Intermodulation atomic force microscopy Appl. Phys. Lett. 92 153106
- [11] Hutter C, Platz D, Tholén E A, Hansson T H and Haviland D B 2010 Reconstructing nonlinearities with intermodulation spectroscopy *Phys. Rev. Lett.* 104 050801
- [12] Berg J and Briggs G A D 1997 Nonlinear dynamics of intermittent-contact mode atomic force microscopy *Phys. Rev.* B 55 14899
- [13] Basso M, Giarre L, Dahleh M and Mezić I 1998 Numerical analysis of complex dynamics in atomic force microscopes *Proc. IEEE Int. Conf. Control Appl.* 2 1026–30
- [14] Wolf K and Gottlieb O 2002 Nonlinear dynamics of a noncontacting atomic force microscope cantilever actuated by a piezoelectric layer *J. Appl. Phys.* **91** 4701–9
- [15] Yagasaki K 2004 Nonlinear dynamics of vibrating microcantilevers in tapping-mode atomic force microscopy *Phys. Rev.* B 70 245419
- [16] Hu S and Raman A 2006 Chaos in atomic force microscopy Phys. Rev. Lett. 96 036107
- [17] Jamitzky F, Stark M, Bunk W, Heckl W M and Stark R W 2006 Chaos in dynamic atomic force microscopy Nanotechnology 17 S213–S220
- [18] Zhang Y and Zhao Y 2007 Nonlinear dynamics of atomic force microscopy with intermittent contact *Chaos, Solitons Fractals* 34 1021–4
- [19] Yagasaki K 2007 Bifurcations and chaos in vibrating microcantilevers of tapping mode atomic force microscopy Int. J. Non-Linear Mech. 42 658–72
- [20] Raman A, Melcher J and Tung R 2008 Cantilever dynamics in atomic force microscopy *Nano Today* **3** 20–7
- [21] Pai N, Wang C and Lin D T W 2010 Bifurcation analysis of a microcantilever in AFM system *J. Franklin Inst.* 347 1353–67
- [22] Stark R W 2010 Bistability, higher harmonics and chaos in AFM *Mater. Today* 13 24–32
- [23] Platz D, Forchheimer D, Tholén E A and Haviland D B 2012 The role of nonlinear dynamics in quantitative atomic force microscopy *Nanotechnology* 23 265705
- [24] Yagasaki K 2013 Nonlinear dynamics and bifurcations in external feedback control of microcantilevers in atomic force microscopy Commun. Nonlinear Sci. Numer. Simulation 18 2926–43
- [25] Lee S I, Howell S W, Raman A and Reifenberger R 2002 Nonlinear dynamics of microcantilevers in tapping mode atomic force microscopy: A comparison between theory and experiment *Phys. Rev.* B 66 115409
- [26] San Paulo A and García R 2001 Tip-surface forces, amplitude and energy dissipation in amplitude-modulation (tapping mode) force microscopy *Phys. Rev.* B 64 193411
- [27] Stark M, Stark R W, Heckl W M and Guckenberger R 2002 Inverting dynamic force microscopy: From signals to

- time-resolved interaction forces *Proc. Natl Acad. Sci. USA* **99** 8473–8
- [28] Stark R W and Heckl W M 2000 Fourier transformed atomic force microscopy: tapping mode atomic force microscopy beyond the Hookian approximation Surf. Sci. 457 219–28
- [29] Rodrguez T R and Garca R 2002 Tip motion in amplitude modulation (tapping-mode) atomic-force microscopy: Comparison between continuous and point-mass models Appl. Phys. Lett. 80 1646–8
- [30] Sahin O, Magonov S, Su C, Quate C F and Solgaard O 2007 An atomic force microscope tip designed to measure time-varying nanomechanical forces *Nat. Nanotechnol.* 2 507–14
- [31] Sahin O 2008 Time-varying tip-sample force measurements and steady-state dynamics in tapping-mode atomic force microscopy *Phys. Rev.* B 77 115405
- [32] Sahin O and Erina N 2008 High-resolution and large dynamic range nanomechanical mapping in tapping-mode atomic force microscopy *Nanotechnology* **19** 445717
- [33] Sarioglu A F and Solgaard O 2008 Cantilevers with integrated sensor for time-resolved force measurement in tapping-mode atomic force microscopy *Appl. Phys. Lett.* 93 023114
- [34] Sarioglu A F, Liu M and Solgaard O 2011 High-resolution nanomechanical mapping using interferometric-force-sensing afm probes *J. Microelectromech. Syst.* 20 654–64
- [35] Sarioglu A F and Solgaard O 2011 Modeling, design and analysis of interferometric cantilevers for time-resolved force measurements in tapping-mode atomic force microscopy J. Appl. Phys. 109 064316
- [36] Sarioglu A F, Magonov S and Solgaard O 2012 Tapping-mode force spectroscopy using cantilevers with interferometric high-bandwidth force sensors Appl. Phys. Lett. 100 053109
- [37] Vijayraghavan K, Wang A, Solgaard O, Butte M J and Melosh N A 2013 Measurement of elastic properties in fluid using high bandwidth atomic force microscope probes Appl. Phys. Lett. 102 103111
- [38] Shaik N, Reifenberger R G and Raman A 2016 Enhancing the optical lever sensitivity of microcantilevers for dynamic atomic force microscopy via integrated low frequency paddles *Nanotechnology* 27 195502
- [39] Legleiter J, Park M, Cusick B and Kowalewski T 2006 Scanning probe acceleration microscopy (spam) in fluids: mapping mechanical properties of surfaces at the nanoscale *Proc. Natl Acad. Sci. USA* 103 4813–18
- [40] Herruzo E T, Perrino A P and Garcia R 2014 Fast nanomechanical spectroscopy of soft matter *Nat. Commun.* 5 3126
- [41] Thota P, MacLaren S and Dankowicz H 2007 Controlling bistability in tapping-mode atomic force microscopy using dual-frequency excitation Appl. Phys. Lett. 91 093108
- [42] Kiracofe D, Raman A and Yablon D 2013 Multiple regimes of operation in bimodal afm: understanding the energy of cantilever eigenmodes *Beilstein J. Nanotechnol*. 4 385–93
- [43] Raman A, Trigueros S, Cartagena A, Stevenson A P Z, Susilo M, Nauman E and Contera S A 2011 Mapping nanomechanical properties of live cells using multi-harmonic atomic force microscopy *Nat. Nanotechnol.* 6 809–14
- [44] Cartagena A, Hernando-Pérez M, Carrascosa J L, de Pablo P J and Raman A 2013 Mapping in vitro local material properties of intact and disrupted virions at high resolution using multi-harmonic atomic force microscopy *Nanoscale* 5 4729–36
- [45] (http://brukerafmprobes.com/a-3724-ps-ldpe-12m.aspx)

- [46] Melcher J, Hu S and Raman A 2007 Equivalent point-mass models of continuous atomic force microscope probes Appl. Phys. Lett. 91 053101
- [47] Platz D, Forchheimer D, Tholén E A and Haviland D B 2013 Interaction imaging with amplitude-dependence force spectroscopy *Nat. Commun.* 4 1360
- [48] Sader J E, Uchihashi T, Higgins M J, Farrell A, Nakayama Y and Jarvis S P 2005 Quantitative force measurements using frequency modulation atomic force microscopy theoretical foundations *Nanotechnology* 16 S94–S101
- [49] Cleveland J P, Anczykowski B, Schmid A E and Elings V B 1998 Energy dissipation in tapping-mode atomic force microscopy Appl. Phys. Lett. 72 2613–15
- [50] Melcher J, Hu S and Raman A 2008 Invited article: VEDA: A web-based virtual environment for dynamic atomic force microscopy Rev. Sci. Instrum. 79 061301
- [51] Kiracofe D, Melcher J and Raman A 2012 Gaining insight into the physics of dynamic atomic force microscopy in complex environments using the VEDA simulator *Rev. Sci. Instrum.* 83 013702

- [52] Kiracofe D, Melcher J, Raman A, Balasubramaniam S, Johnson S D and Hu S 2012 VEDA: Virtual environment for dynamic AFM
- [53] Derjaguin B V, Muller V M and Toporov Y P 1975 Effect of contact deformations on the adhesion of particles *J. Colloid Interface Sci.* 53 314–26
- [54] Zhang Y 2011 Adhesion map of spheres: Effects of curved contact interface and surface interaction outside contact region J. Adhes. Sci. Technol. 25 1435–64
- [55] Attard P 2007 Measurement and interpretation of elastic and viscoelastic properties with the atomic force microscope J. Phys.: Condens. Matter. 19 473201
- [56] Rajabifar B, Jadhav J M, Kiracofe D, Meyers G F and Raman A 2018 Dynamic afm on viscoelastic polymer samples with surface forces *Macromolecules* 51 9649–61
- [57] Crittenden S 2005 Intrinsic harmonic distortion of atomic force microscopy cantilever position detection methods Asme Proceedings, Design Engineering, Parts A and B pp 469–74